Journal of Materials Chemistry C

ROYAL SOCIETY OF CHEMISTRY

PAPER

View Article Online
View Journal | View Issue

Cite this: J. Mater. Chem. C, 2025, 13, 1243

Unexpected piezoelectric properties of electrospun polyimide nanofibers for application in an extreme environment

Liangkang Huang,[a] Jianwei Li,*[ab] Shuting Chen,[a] Bilin Zhang,[a] Shengping Li,[a] Wei Fan,[c] Qiangli Zhao[a] and Xuman Wang[a]

Received 27th August 2024,
Accepted 30th October 2024

DOI: 10.1039/d4tc03656e

rsc.li/materials-c

Developing a piezoelectric polymer with high-temperature resistance is crucial for fabricating flexible piezoelectric sensors that can be used under extreme conditions. Herein, we for the first time found the piezoelectric properties of polyimide (PI) nanofibers and further enhanced their output voltage characteristics by introducing a fluorine-containing hexafluorodianhydride (6FDA) unit into the PI nanofibrous matrix. The as-fabricated sensor can produce a stable piezoelectric output of 10 V with a 478.72 mV N^{-1} sensitivity. The response and recovery times are 15 ms, respectively, and the output can remain stable after 10,000 cycles at 15 Hz/10 N, demonstrating excellent durability. Meanwhile, the 10–30 V piezoelectric output signals generated by different actions can be accurately identified for wearable applications. Furthermore, it is found that fluorinated polyimide (FPI) prepared by electrospinning can maintain structural stability before 500 °C, and its thermal decomposition temperature is above 550 °C. Moreover, the surface morphology with high porosity and the low surface energy of F atoms endow the nanofiber film with excellent superhydrophobic properties with a water contact angle of 139.6°. This work presents PI nanofibers with high-temperature resistance and outstanding piezoelectric properties, laying a potential foundation for their application in wearable and flexible electronic devices that can be used in extreme environments.

Introduction

Piezoelectric materials can convert mechanical stress into an electric field, which makes them widely used in sensors and energy-collection devices.[1] Traditional piezoelectric materials, such as some ceramic materials, lose their piezoelectric properties at high temperatures, limiting their use in some application scenarios that need high-temperature operation.[2] High-temperature-resistant piezoelectric materials have various potential applications in extreme environments, covering aerospace, oil and gas, automobile, metallurgy, and other industries. The reliability and effectiveness of these materials will help improve equipment performance, ensure safety and efficiency, and promote the development of related technologies. A high-temperature resistant piezoelectric polymer is a material that can maintain good piezoelectric properties in a high-temperature environment.[3] Research into high-temperature resistant piezoelectric polymers mainly focuses on improving the thermal stability of the materials.[4,5] In addition, studies also involved developing new polymers and adjusting the structure and chemical composition of the existing piezoelectric polymers, such as polyvinylidene fluoride (PVDF) and polyacrylonitrile (PAN).[6–11] With the development of materials science and polymer chemistry, many high-temperature resistant piezoelectric polymers or composites to meet special industrial applications were fabricated.[12,13] The improvement of these materials can not only expand their application scope but also improve the reliability and efficiency of equipment in extreme environments.

PVDF is a widely used piezoelectric polymer material with excellent chemical resistance, wear resistance, aging resistance, and piezoelectric properties.[14,15] It is a semi-crystalline polymer with high crystallinity and molecular weight, and can be made into films, nanofibers, and plates by drawing, electrospinning, or calendering. Guo *et al.*[16] prepared a flexible PVDF/$BaTiO_3$ three-dimensional porous composite foam with a melting temperature of about 145 °C by supercritical carbon dioxide ($scCO_2$) foaming technology and surface modification. The piezoelectric output is increased to 12.5 V and 150 nA, and the peak output power density is 0.15 μW cm^{-2}, which is 25 times that of a flat film.

[a] School of Materials Science and Engineering, Key Laboratory of Functional Textile Material and Product of Ministry of Education, Xi'an Polytechnic University, Xi'an, 710048, China. E-mail: lijianwei@xpu.edu.cn
[b] National Advanced Functional Fiber Innovation Center, Suzhou, 215000, China
[c] School of Textile Science and Engineering, Xi'an Polytechnic University, Xi'an, 710048, China

Song *et al.*[17] reported that a layered nested network was constructed in PVDF foam using solid-state shear crushing and salt leaching technology. The melting temperature of the prepared bubble is 170 °C, and the maximum piezoelectric output voltage reaches 11.84 V and 217.78 nA, respectively. Because the crystalline orientation of PVDF began to weaken at a melting point of 170 °C, it lost its original structure, so the piezoelectric properties started to decline at 80 °C.[18] To sum up, the PVDF material has specific temperature-resistant piezoelectric properties, and it can still maintain its piezoelectric properties at medium and low temperatures, so it has broad prospects for piezoelectric applications and can be applied in some medium and low-temperature environments.

PAN is also one of the polymers reported to exhibit both high-temperature resistance and piezoelectric properties.[7,19] PAN is a polymer material with good piezoelectric performance.[6,20] PAN has a highly polarized structure, which gives it excellent piezoelectric and mechanical properties.[21,22] Its piezoelectric properties can be adjusted by changing the structure of the material and adding specific additives, making it widely used in electronics, communications, medical care, and automobiles. It also provides essential support for modern science and technology development. Fu *et al.*[20] reported that an electrospun PAN/$BaTiO_3$/MXene nanofiber membrane with a decomposition temperature of 230 °C was obtained by introducing $BaTiO_3$ and MXene (Ti_3C_2) PAN, which had significantly enhanced piezoelectric properties compared with those of a pure PAN nanofiber membrane. Zheng *et al.*[23] reported that a thermally stable PAN nanofiber membrane prepared by electrospinning and heat treatment procedures can effectively and stably convert thermoacoustic waves into considerable electric energy at temperatures as high as 450 °C. In contrast, the non-heat-treated PAN nanofiber membrane becomes unstable after working for only 40 s at 200 °C. For amorphous polymer PAN, the order of dipole groups decreases at T_g temperature, and the piezoelectric properties become weak due to the conformation transformation. To sum up, PAN has a specific high-temperature piezoelectric resistance, and is suitable for piezoelectric applications and testing within a particular range of medium and high-temperature environments.[19,24] However, selecting the appropriate materials according to specific high-temperature conditions and requirements is necessary to ensure the stability and reliability of piezoelectric properties.

To sum up, developing a new type of piezoelectric polymer that can resist high temperatures and produce piezoelectric signals is essential. PI is a high-performance polymer that has attracted much attention due to its excellent high-temperature resistance.[25,26] It has excellent thermal stability and shows stable physical and chemical properties at extreme temperatures.[27,28] This kind of material not only has exceptional properties that common polymer materials cannot match but can also be widely used in aerospace, electronics, and many other fields.[29,30] It has also become a critical material for promoting scientific and technological progress.[31,32] Therefore, a novel piezoelectric polymer fluorine-containing polyimide (FPI) with a thermal decomposition temperature higher than 500 °C was prepared by introducing a polar atom, fluorine, into polyimide (PI).[33,34] In addition, FPI is not only high-temperature resistant but also has piezoelectric characteristics. A piezoelectric signal of 10–30 V can be generated using the FPI nanofiber membrane. The FPI nanofiber membrane has excellent chemical stability and mechanical and electrical properties simultaneously. It is an ideal material choice for various fields that need high-temperature resistance. Therefore, the research of high-temperature resistant nanofibers for application in wearable and flexible sensors is of great significance to advancing science and technology and will provide new solutions for monitoring extreme high-temperature environments in medical treatment, health monitoring, and intelligent wearable devices.

Experimental section

Materials

Monomer 4,4 ether (ODA, ≥98.0%), 3,3′,4,4′-benzophenone tetramethyl acid dianhydride (BTDA, ≥99.0%), and 4,4′-(hexafluoroisopropylidene) phthalic anhydride (6FDA, ≥99.0%) were used. *N*,*N*-Dimethylformamide (DMF, ≥99.5%, AR) was purchased from Shanghai Aladdin Industrial Co. Ltd (Shanghai, China). All reagents are analytically pure and have not been further processed before use.

Preparation of polyimide nanofiber films and their sensor

The nanofiber membranes prepared in this work are fluorine-containing polyimide (FPI) with different fluorine contents. Firstly, a fluorinated polyamic acid (FPAA) prepolymer solution for electrospinning was prepared. 40 mL of DMF and 0.015 mol of ODA were added in a three-necked flask and stirred for 30 minutes until ODA was fully dissolved. Subsequently, 6FDA and BTDA in a total quantity of 0.015 mol were added, and the reaction was conducted in an ice-water bath for 12 hours, forming the FPAA solution. Five kinds of spinning solutions with different fluorine contents were prepared by adjusting the molar ratios of BTDA to 6FDA of 1 : 0, 8 : 2, 6 : 4, 4 : 6, and 0 : 1, respectively. The obtained FPAA solution was transferred to a 10 mL syringe for electrospinning. The spinning voltage was 20 kV, the spinning speed was 1 mL h^{-1}, and the spinning distance was 15 cm, respectively. Finally, the spinning film was heated to 260 °C in an oven by gradient thermal imidization to form FPI, and its fabrication process is shown in Fig. 1b. The fluorine-containing nanofiber membranes with different proportions were named PI-0, FPI-0.2, FPI-0.4, FPI-0.6, and FPI-1.0, respectively, according to the relative content of 6FDA.

The flexible nano piezoelectric sensor prepared in this paper comprises a sandwich structure with five layers. First, an FPI nanofiber membrane slightly more extensive than 3 × 3 cm^2 and two 3 × 3 cm^2 copper foils (with a thickness of 50 μm) is taken, and wires are connected to the two copper foils. Then, the nanofiber membrane is sandwiched between two pieces of copper foil so the charge can be smoothly extracted from the two copper electrode plates. Finally, a layer of the Kapton PI film slightly more extensive than 3 × 3 cm^2 was pasted on the

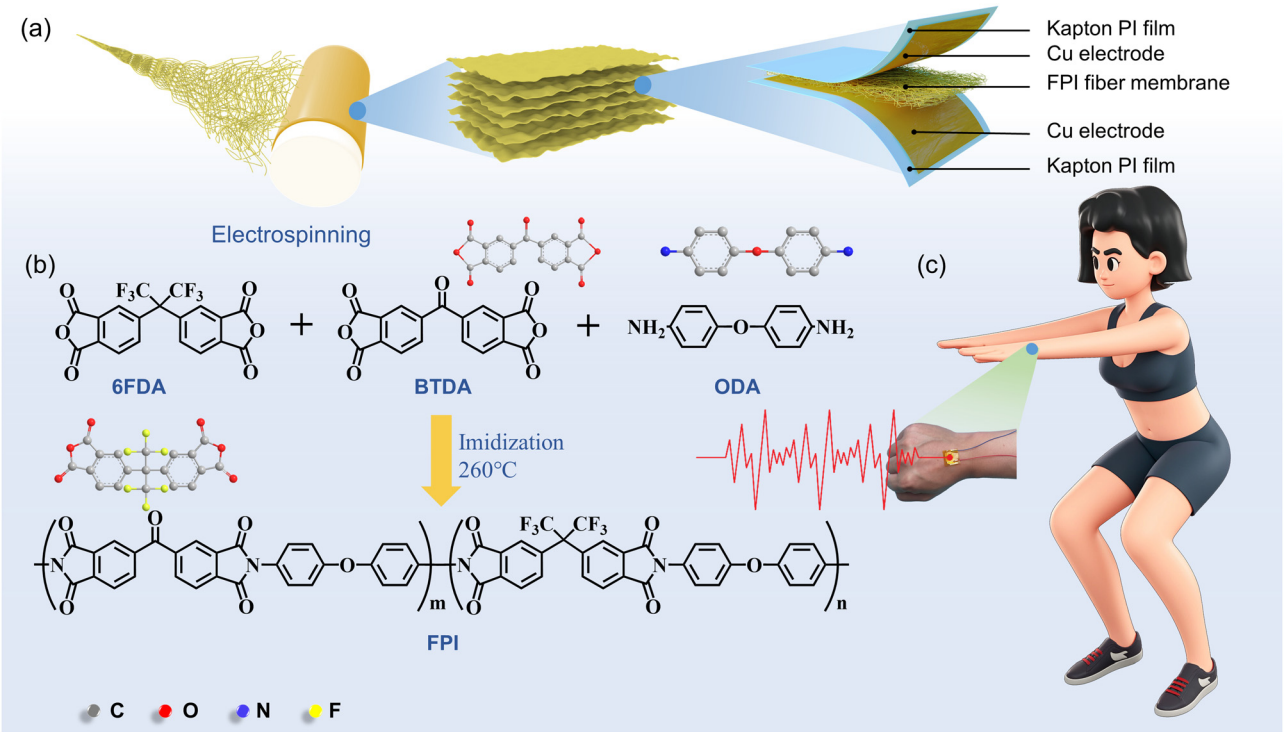

Fig. 1 Schematic diagram of preparation and application of a flexible nano-piezoelectric sensor. (a) Preparation of a flexible sensor by electrospinning. (b) The reaction principle of synthesizing FPI. (c) Testing of wearable applications.

copper electrode in the same method, and a piezoelectric sensor was fabricated (Fig. 1a).

Characterization

The microstructure of the FPI nanofiber membrane was analyzed using a scanning electron microscope (SEM, TESCAN MIRA, Czech Republic). The distribution and content of elements in the FPI nanofiber membrane were analyzed using an X-ray energy spectrometer (EDS, OXFORD XPLORE-30, UK). The chemical structure of the FPI nanofiber membrane was characterized using a Fourier transform infrared spectrometer (FT-IR, TENSOR-27, Bruker, USA). The scanning wave number was 400–3000 cm^{-1}. An X-ray diffractometer (XRD, DX-2700 BH, Haoyuan Instrument) was used to record the X-ray diffraction patterns of the nanofiber membrane. A universal testing machine was used to test the tensile properties of the nanofiber films. A thermogravimetric analyzer (TGA, STA 449 F5, Germany) was used to test the thermal stability of the nanofiber membrane. An electrometer (Keithley 6514) was used to collect the voltage signals generated after the vibration exciter excited the sample.

Results and discussion

The fabrication and structure of nanofibrous films

Electrospinning is an effective technique for preparing nanofibrous membranes.[35,36] This preparation method is simple in operation, low in cost, and fast in preparation, so it has been widely used in the field of materials science. The nanofiber membrane prepared using this method has a large specific surface area and porosity, making it has a significant application value in sensing. Moreover, adjusting the spinning voltage, speed, distance, temperature, and humidity can customize the nanofiber's diameter, density, and performance. Fig. 2a shows the cross-sectional micro-morphology of the obtained PI-0 nanofiber membrane. It can be found that the nanofibers have an apparent multilayered structure. On the one hand, during the spinning process, the PAA solution is subjected to an electric field, and the arrangement direction of molecular chains is affected by the electric field force, leading to nanofibers' formation. Due to the high humidity in the spinning process (60–70%), PAA on the surface of nascent nanofibers can be precipitated due to moisture, resulting in the rapid formation of nascent PAA nanofibers in a unit of time. Besides, with the continuous rotation of the collection drum, nanofibers are piled up layer by layer on the drum, and the nanofiber membrane is gradually solidified in a certain period, thus forming this multilayered structure.

Fig. 2b and c show the surface morphology of the PI-0 nanofiber membrane. As the rotation direction of the collecting cylinder is always the same during spinning, it can be seen that the nanofibers are arranged in the same direction as a whole. At the same time, the direction of the molecular chains is influenced by electric field force, and a small number of nanofibers also show a staggered arrangement.[37] Moreover, these staggered nanofibers on the surface present a rich micro–nano structure. These abundant micro-morphological characteristics

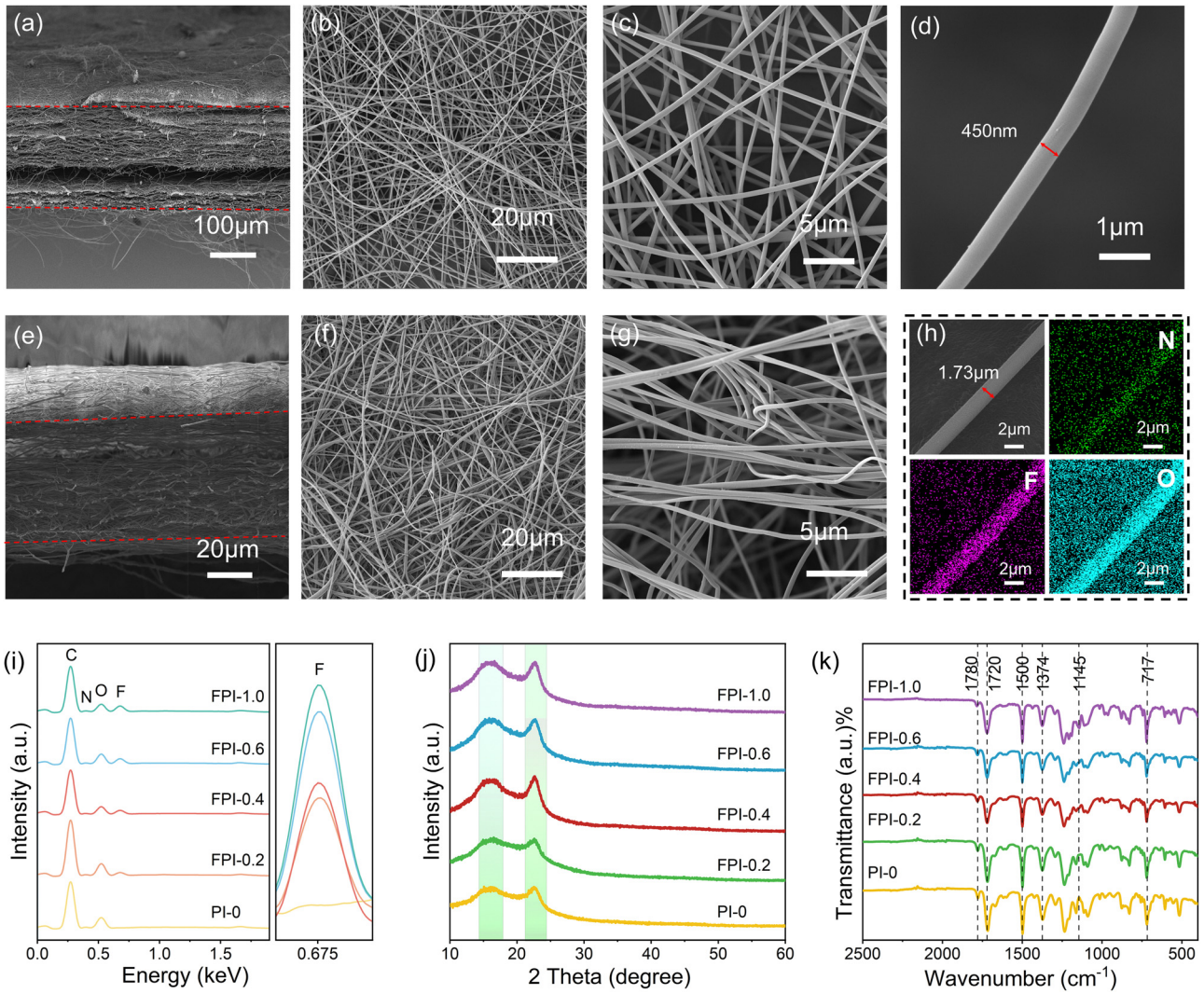

Fig. 2 Microscopic characterization of the FPI nanofiber membrane. (a)–(g) Scanning electron microscopy (SEM) images show the micro-morphology of the composite nanofiber membrane of FPI-*x*. (h) The distribution of elements in the FPI nanofiber membrane. (i) EDS energy spectrum of the FPI nanofiber membrane. (j) XRD spectra of the FPI nanofiber membrane. (k) The FT-IR spectrum of the FPI nanofiber membrane.

reflect the complex hydrodynamics and electric field effect in the spinning process and directly affect the crucial properties of the membrane material, such as pore structure, specific surface area, and wettability. The morphology of the PI-0 single nanofiber is displayed in two dimensions (Fig. 2d). As can be seen, the surface of the prepared nanofibers is smooth, there are no beaded droplets, and the diameters are all around 450 nm. Compared with FPI (Fig. 2h), the introduction of fluorine influences the fiber diameter. Of course, these changes are also closely related to electrospinning parameters. The structural characteristics of fluorine can affect the viscosity and fluidity of the electrospinning solution, thus affecting the spinning process and the final fiber morphology of the nanofibers.

Fig. 2e shows the cross-sectional micro-morphology of the FPI nanofiber membrane. Due to the same spinning process, the cross-sectional micro-morphology of the FPI nanofiber membrane and the PI-0 nanofiber membrane is very similar and shows stratification characteristics. Fig. 2f and g show the surface micro-morphology of the FPI nanofiber membrane. Compared with the morphology of PI-0, the arrangement of nanofibers of the FPI nanofiber is more chaotic. Because of the introduction of fluorine-containing groups and the influence of the electrostatic field, the force between nanofibers increases, which makes the arrangement and orientation of FPI nanofibers more chaotic. Fig. 2h shows the element distribution of N, F, and O in a single FPI nanofiber. It can be seen that the elements are evenly distributed on the nanofiber, in which N belongs to the amino group in ODA. F belongs to the $-CF_3$ group in 6FDA. The content of the N element in the whole molecular chain is shallow. It is observed from the distribution of the F element in the nanofiber that the F element has been successfully introduced into the polyimide molecular chain. Fig. 2i shows the EDS energy spectra of PI-0, FPI-0. 2, FPI-0. 4, FPI-0.6, and FPI-1.0. The energy spectra for comparing the F-element content were scanned for four elements: C, N, O, and F. Among them, the content of element C is the highest,

which is attributed to the C main chain of organic matter. With the gradual increase of the 6FDA content in the molecular chain, the content of the F element shows an increasing trend, further proving that the F element has been successfully introduced into the polyimide molecular chain.

The loose molecular chain stacking observed in PI resin significantly affects its solubility. This loose packing is mainly due to $-CF_3$ substituents in the dianhydride, which increases the distance between molecular chains.[38,39] These structural characteristics make the nanofiber membranes amorphous. The polymer backbone with a plurality of $-CF_3$ groups reduces chain–chain interactions and chain stacking effects, which prevents the polymer from crystallizing. The XRD results in Fig. 2j show that two X-ray absorption peaks are observed in the scattering angle (θ) range of 10–60° for all samples. The FPI spun film shows a broader scattering peak at 2θ = 15–20°, revealing an amorphous structure in the FPI nanofibers. A distinct diffraction peak appeared at $2\theta = 22.57°$, corresponding to the (110) crystal plane. This result suggests that the FPAA solution was subjected to high stretching during electrostatic spinning and polarized under high-voltage electric field conditions, transforming the molecular chains of the otherwise loose FPI nanofibers toward a crystalline structure.

The chemical structure of the prepared sample was analyzed by FT-IR (Fig. 2k). The peak near 1780 cm^{-1} belongs to the asymmetric stretching vibration of C=O. The peak near 1720 cm^{-1} belongs to the symmetric stretching vibration of C=O. The peak at 1500 cm^{-1} belongs to the stretching vibration of the resonant C=C double bond on the benzene ring. The peak at around 1560 cm^{-1} belongs to the N–H telescopic vibration. The peak near 1374 cm^{-1} belongs to the stretching vibration of C–N.[40] The peak near 1145 cm^{-1} belongs to the stretching vibration of the C–F bond on the benzene ring in 6FDA. The comparison of the peak heights of the C–F bond shows that the absorption peak near 1145 cm^{-1} is more and more significant with the increase of the fluorine atom content.[41] Moreover, the characteristic absorption peak of PAA is not observed, which indicates that PAA was completely cured to polyimide.

The mechanical and thermal properties

Nanofibers are widely used in bio-sensing and other fields, and their mechanical properties directly affect their stability and reliability.[42] The study of the mechanical properties of nanofibers can facilitate a better understanding of their properties and potential for various applications.[43] Therefore, the mechanical tensile strength of FPI nanofiber films with different fluorine percentages was tested, and the tensile stress–strain curves are shown in Fig. 3a. The figure shows that all the FPI nanofiber membranes exhibit typical plastic deformation behavior during the tensile process and all present a rapid increase in stress.[44] Among them, PI-0 and FPI-0.2 show higher elongation at break. With the increase of the $-CF_3$ content, the elastic modulus of the sample shows a downward trend (Fig. 3c). In addition, with the increase of the $-CF_3$ content, the tensile strength of the sample gradually decreases, showing a downward trend (Fig. 3b). This phenomenon is mainly due to the molecular chains' stacking arrangement degree and reduced molecular weight. Upon increasing the 6FDA content, the solid electron-absorbing effect of $-CF_3$ makes the reactivity of the dianhydride not strong, and thus, the molecular weight of the system is low, and the molecular chain is short.[38] On the other hand, with the increase of the fluorine content in the system, $-CF_3$ hindered the accumulation of molecular chains, making the distance between molecular chains larger. Therefore, the slighter intermolecular force and the lower packing density lead to a downward trend in elastic modulus and tensile strength.[45]

The excellent mechanical strength and thermal stability make PI an indispensable engineering plastic with high performance. However, it is necessary to comprehensively test the thermal characteristics of PI nanofibrous films to ensure their reliability and service life under different operating conditions. As a standard thermal analysis technology, differential scanning calorimetry (DSC) can be used to effectively test and evaluate the thermal behavior of polyimide, including the glass transition temperature, thermal stability, and other vital parameters, as shown in Fig. 3d. The results demonstrate that the glass transition temperature (T_g) of the FPI prepared in this study is slightly higher than 260 °C. Compared with PVDF and PAN, FPI prepared in this study has a higher T_g value, indicating that it is suitable for a higher-temperature environment. Through comprehensive analysis of the test data, the thermal properties of PI can be accurately determined, which provides valuable insights for the optimization design and performance prediction of polyimide in high-performance applications. High-temperature resistance analysis is a crucial tool for assessing the performance of PI materials under extreme conditions, and studying their thermal stability provides a comprehensive understanding of their performance in high-temperature environments. The correlation thermogravimetric analysis (TGA) curves of FPI thin films were obtained under a N_2 atmosphere (Fig. 3e). It can be seen that before 500 °C, the thermogravimetric curve is relatively flat, indicating that there are fewer small molecules in the FPI nanofiber film and the thermal imidization is more thorough. Fig. 3f demonstrates the DTG curves of PI-0 and FPI-0.4, and FPI shows that their fastest thermal decomposition temperatures are 588 °C, 609 °C, and 557 °C, respectively. According to Fig. 3f, the nanofiber membranes have good thermal stability, reaching 500 °C at most. Analyzing high-temperature resistance can provide a scientific basis and technical support for the design and application of PI and promote its development and application in various fields.

The high density and slender shape of nano-scale nanofibers make the film able to withstand significant elongation when stressed. In addition, nanofiber membranes have excellent surface flatness and uniformity, making them perform better in practical applications. The FPI nanofibrous film produced by electrostatic spinning is shown in Fig. 3g. Due to the layer-by-layer accumulation of abundant nanofibers generated during the spinning process, the surface is very flat and uniform, accompanied by abundant micro-nanostructures. Fig. 3h illustrates that after curing at 260 °C, the FPI nanofibrous

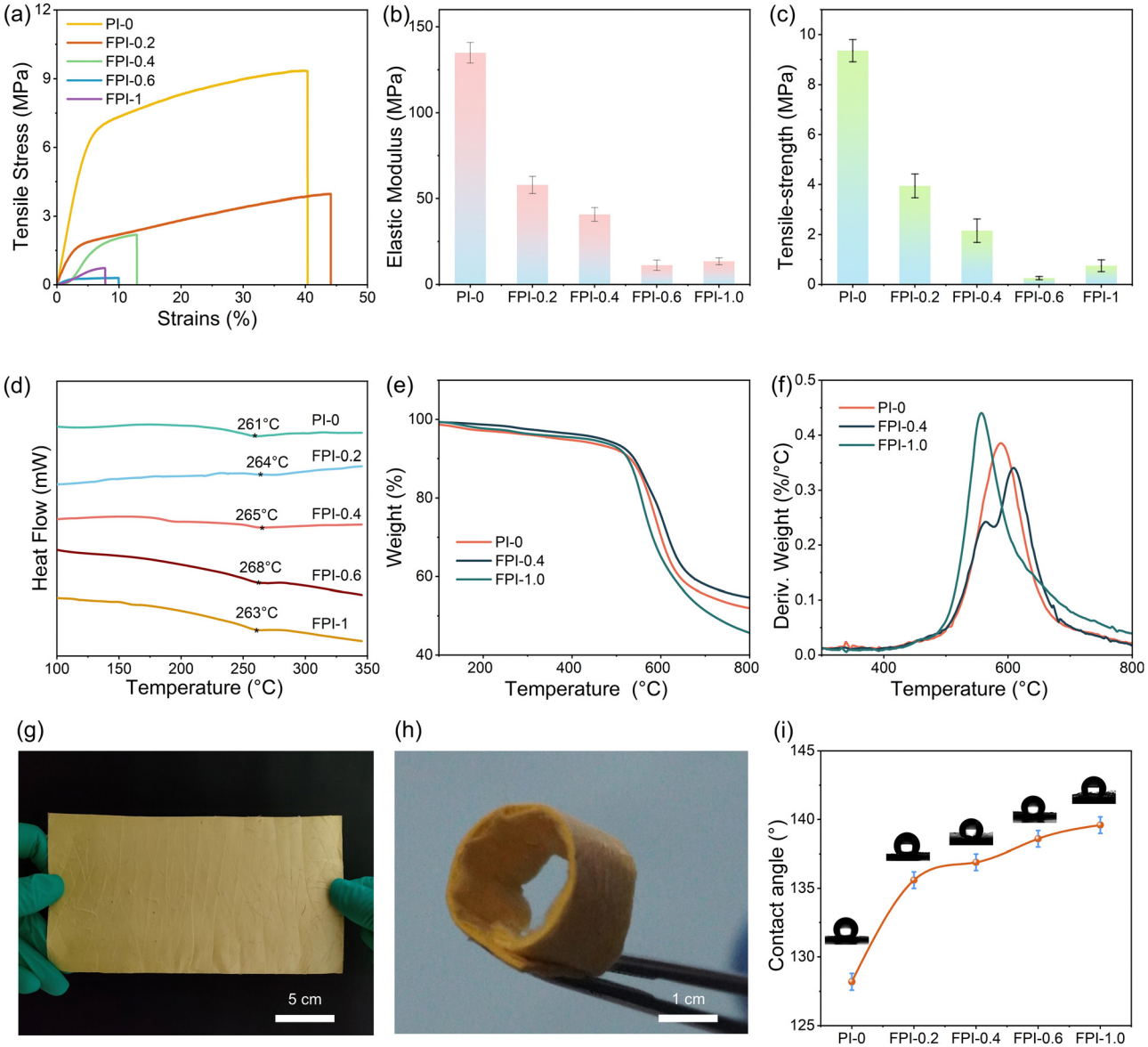

Fig. 3 Characteristics of the PI nanofiber membrane. (a) Tensile test of different FPI nanofiber films. (b) and (c) Tensile strength and modulus of different FPI nanofiber membranes. (d) DSC curves of different FPI nanofiber membranes. (e) and (f) TG and DTG curves of nanofiber membranes. (g) and (h) The photograph shows the optical appearance and flexibility of the nanofiber film. (i) Water contact angle of different FPI nanofiber membranes.

membrane can still be bent at will. Its excellent flexibility enables it to adapt to complex surface shapes while maintaining stability and reliability. The water contact angle for FPI nanofiber membranes is presented in Fig. 3i. The figure shows that the nanofiber membranes with varying fluorine contents exhibit substantial contact angles, with an increase in the contact angle corresponding to the increase in the fluorine content. It can be seen from the Cassie–Baxter equation that the contact angle of the droplets should be increased. Efforts should be made to increase the value of the roughness factor r, which usually requires the preparation of micro-and nano-structures on the object's surface.[46] Fig. 2f demonstrates that the spun films prepared in this study are characterized by high-density micro and nano-structures, as proved by the test result of 128.19°. In contrast, fluoropolymers show low surface tension, low surface energy, and chemical inertia. The critical surface tension of $-CF_3$ is 6 mN m^{-1}, much lower than that of ordinary alkyl groups. The low surface energy of the fluorinated polymer is mainly due to the unique chemical properties of elemental fluorine.[47] Fluoride is the most electronegative element. This is due to the significant difference in electronegativity and the lone pair on the fluorine atom. The bond energy of the C–F bond (485 kJ mol^{-1}) is much greater than that of the C–H bond (413 kJ mol^{-1}). The shielding effect of fluorine atoms makes the fluoropolymer highly chemically inert. With the introduction of fluorine atoms, the contact angle of water increased significantly from 128.19° to 135.59° and then increased to 139.59° with the increase of the fluorine atom content. FPI nanofiber

membranes have great potential for application in the field of hydrophobic materials.

The piezoelectric properties of nanofibrous films

Piezoelectric sensors based on polymeric nanofibers have been extensively studied recently.[48,49] Piezoelectric sensors can convert external mechanical stimuli into electrical signals and have diverse applications across numerous fields.[50,51] In addition, the sensitivity and response speed of the sensors can be effectively improved by using nanofibers as sensitive materials. The piezoelectric properties of nanomaterials are related to the total dipole moment of the materials.[52] By expanding molecular polarization,[53] the piezoelectric output of the nanocomposite films can be improved, which is also applicable to FPI-based piezoelectric nanocomposites.[54,55] As shown in Fig. 4a, the sensor test equipment includes a signal generator and a power amplifier, which cooperate to adjust the excitation behavior generated by the mode vibrator. An electrometer (Keithley 6514) captures the voltage signal the applied pressure generates when the oscillator vibrates the sample.

In their natural state, all kinds of particles inside are in irregular motion, which is not manifest as external electrical properties. However, this paper uses electrostatic spinning to prepare an FPI nanofiber membrane so that the electric dipole inside the material rotates and keeps the same direction as the rotating electric field, thus forming a dipole charge inside the dielectric. Conversely, element F is the most electronegative and active element in nature, exhibiting an electron-inducing solid effect. Therefore, it plays a vital role in enhancing the electronegativity and electron-trapping ability of the FPI nanofiber membrane. An increase in the polar atom content will attract more external electrons, and the increase in the electron number will lead to more significant potential differences. PENG introduced in this paper consists of a substrate, FPI nanofiber membrane, and copper electrodes on both sides. The working mechanism of the encapsulated PENG is shown in Fig. 4b. When an external force acts on the PENG, the FPI nanofiber membrane is induced to produce dipole polarization. The regular arrangement of the dipoles will attract electrons, thus creating a potential difference.

In summary, this work investigates the piezoelectric response law of polar atoms with different concentrations. The d_{33} value of FPI-1 is 3.4 pC N^{-1}. Under the same excitation (10 N, 10 Hz), the piezoelectric signals generated by FPI sensors with varying fluorine contents are shown in Fig. 4c and g. It can be seen that the electrical signal sensitivity of FPI sensors increases with the increase of the concentration of fluorine-containing functional groups under the same external mechanical stress. This is because $-CF_3$ in the 6FDA molecule inside FPI itself has a steric hindrance effect, resulting in a large number of free volume inside the molecule. Due to the free volume of $-CF_3$, the FPI nanofiber membrane is more polarized than the non-fluorinated PI nanofiber membrane when subjected to the same external mechanical stress. The output piezoelectric signal of the non-fluorinated PI nanofiber membrane is 6.3 V. Due to the introduction of fluorine atoms, the nanofiber membrane's ability to attract external electrons is increased, and the output piezoelectric signal gradually increases to 10 V. The current signal also increases from 40 nA to 100 nA with the increase of the fluorine content. The piezoelectric signals generated by the FPI sensors under different pressures at 10 Hz are shown in Fig. 4d and h. The influence of molecular chain polarization is more evident at higher pressures, which will attract more electrons. With the gradual increase in pressure, the output piezoelectric signal is also more intense, increasing from 6.3 V to 10 V. The current signal also presents a rising process. Fig. 4e and i show the piezoelectric response of the FPI sensor under the excitation of different frequencies of 10 N. The faster the excitation, the quicker the polarization of the materials. The more dipoles produced, the more electrons attracted and the stronger the piezoelectric signal output. However, due to the tunnelling current effect, the material limits the velocity of electrons, so the piezoelectric signal will also have a threshold.

Sensitivity, response/recovery time, and stability are the characteristics of the sensor's response to mechanical forces. The sensitivity curve of the FPI sensor is shown in Fig. 4f. The piezoelectric response of the FPI sensor was tested in the pressure range of 5 N to 10 N. The sensitivity obtained by fitting the test data is 478.72 mV N^{-1}. Fig. 4j shows the piezoelectric response and recovery time of the FPI sensor under the excitation of 10 Hz/10 N for 15 ms each time, indicating that the sensor can quickly respond to and recover from piezoelectric signals. Fig. 4k shows a stability test of the FPI sensor for 10 000 cycles. The test results show no deviation, which shows that the sensor has good stability and long-term running potential.

Flexible piezoelectric sensors can convert pressure or pressure changes into electrical signals and have many applications in many fields.[56] Fig. 5 shows the application of the FPI nanofiber piezoelectric sensor prepared in this paper for wearable and movement monitoring. The finger-bending signal measured by the sensor is shown in Fig. 5a. When the sensor is attached to the outside of the index finger, the different piezoelectric signals generated by the finger bending and straightening can be read. Fig. 5b shows the wrist bending signal measured by the sensor. When the wrist bends, the sensor will detect the pressure generated by the wrist muscles and then generate the piezoelectric signal. Fig. 5c shows the elbow flexion signal measured by the sensor. During elbow flexion, the elbow presses against the sensor surface. The sensor can accurately read the piezoelectric signal produced by each elbow flexion. From the test, the fabricated sensor will significantly help patients rehabilitate when used in the medical field.

Fig. 5d illustrates the sensor's signal acquisition for three modes of motion: walking, running, and jumping. Because each movement mode produces different frequencies and pressures, it can be observed that different movement modes will produce different signals. When walking, the frequency is slow, and the frequency of the piezoelectric signal generated is slow. However, the piezoelectric signals generated during running are faster than those generated during walking, indicating that the FPI nanofiber piezoelectric sensor prepared in this work can sense different frequencies. In addition, the peak

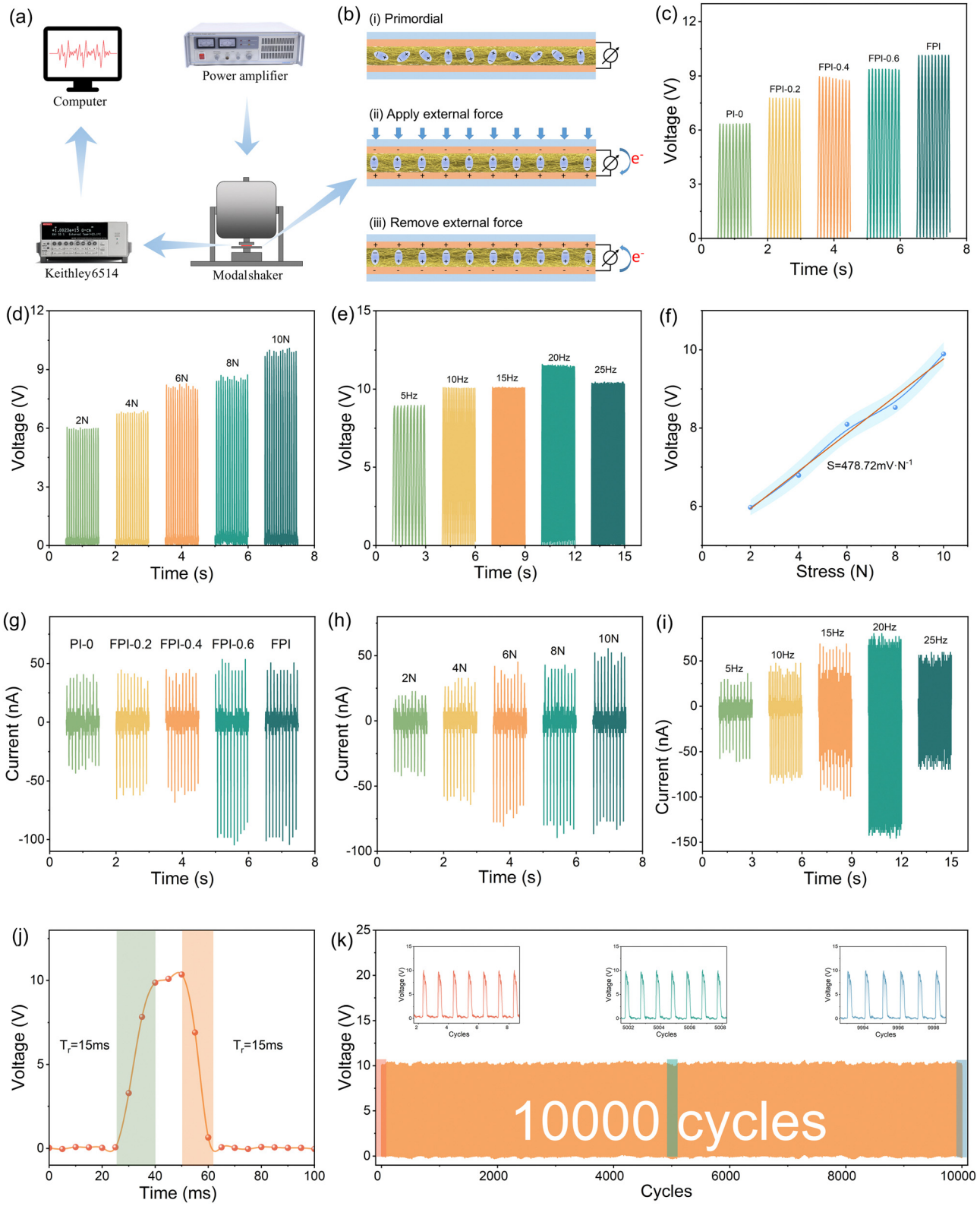

Fig. 4 Dynamic response test of the piezoelectric sensor. (a) FPI sensor signal testing equipment. (b) Schematic diagram of the working principle of the FPI sensor in the pressure/release state. (c) Output voltage responses of different fluorine content sensors under 10 Hz/10 N excitation. (d) The piezoelectric output voltage response of the FPI sensor under different pressure excitations of 10 Hz. (e) Output voltage response of the FPI sensor to varying frequencies of 10 N. (f) Sensitivity curve of the FPI sensor. (g) Output current responses of sensors with different fluorine contents under 10 Hz/10 N excitation. (h) The piezoelectric output current response of the FPI sensor under different pressure excitations of 10 Hz. (i) The output current response of the FPI sensor to 10 N changing frequency. (j) Response time and recovery time of the FPI sensor under 10 Hz/10 N excitation. (k) The durability of the FPI piezoelectric sensor under 10 Hz/10 N excitation.

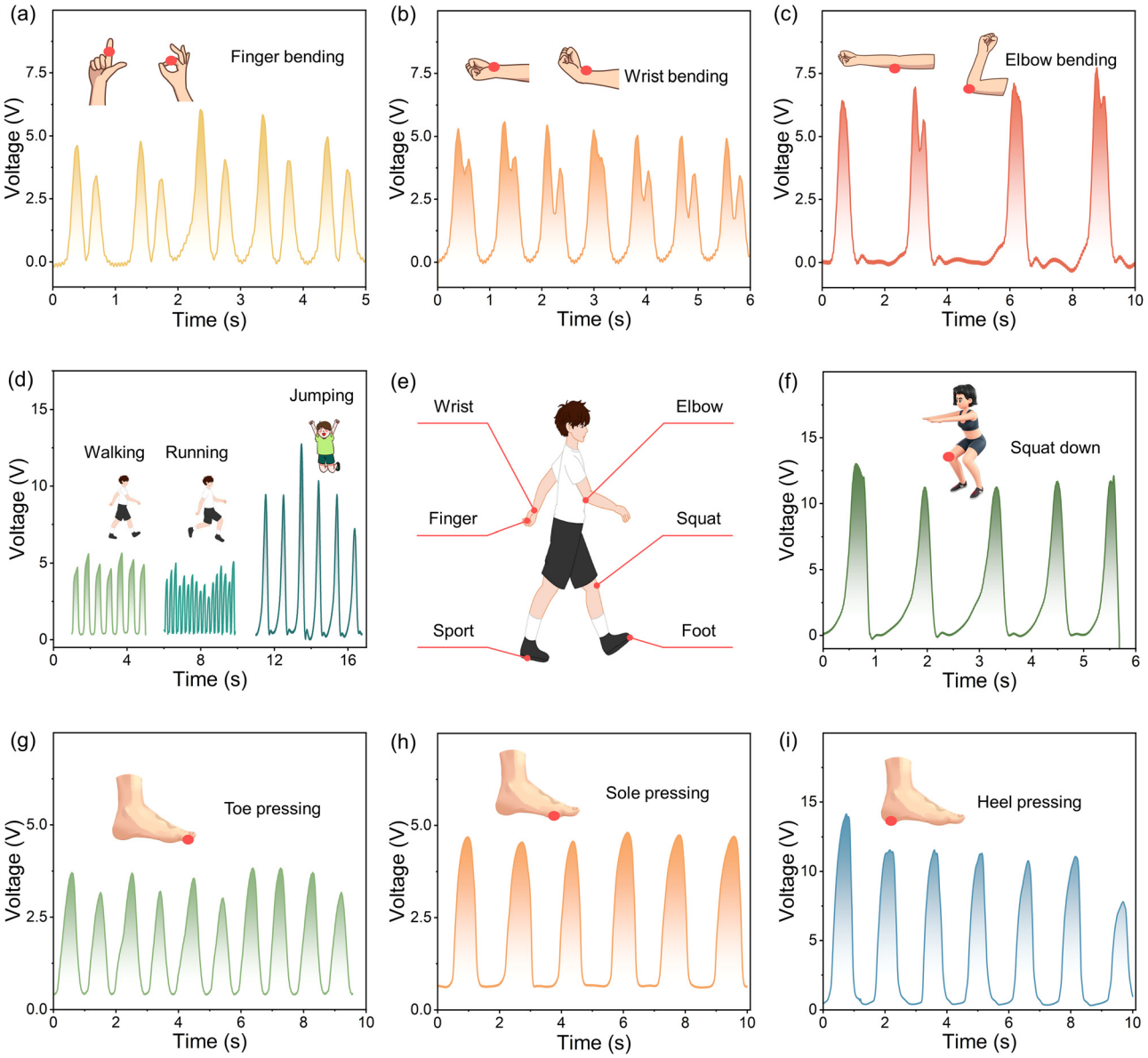

Fig. 5 FPI sensor testing for wearable applications. (a) Finger bending test. (b) Wrist bending test. (c) Elbow bending test. (d) Walking, running, and jumping motion tests. (e) Schematic diagram of sensing on different parts of the human body. (f) Deep squat test. (g) Toe press test. (h) Foot press test. (i) Heel press test.

value of the piezoelectric signals produced by high jump is higher than that produced by walking and running. This is because the human body produces a significant momentum during the process of falling, resulting in pressure exceeding the self-weight of the human body. In comparison, it has been found that the FPI nanofiber piezoelectric sensor can identify the pressure at different frequencies and the pressure at different sizes. Integrating the flexible piezoelectric sensors prepared in this paper into intelligent wearable devices will facilitate monitoring the user's physical activity, sleep quality, physiological indicators, and other pertinent information for health status monitoring and fitness guidance.

A schematic diagram of the sensing of different parts of the test body, including the hand, the wrists, the elbows, the knees, the movement of the joints, and the soles of the feet, is presented in Fig. 5d. Fig. 5f illustrates the piezoelectric signal collected at the knee during deep squatting. When a person squats, the stretching and bending of the skin on the surface of the knee makes the sensor attached to the skin surface press. The sensor will have a significant and promising application in electronic skin. The piezoelectric signals produced by the toe, foot, and heel pressure sensors are shown in Fig. 5g and i, respectively. A comparison of these three pictures reveals the significant differences in piezoelectric signals generated at different positions of the sole. From the perspective of human body mechanics and balance, when a person is standing, the toes, the foot, and the heel are subjected to different pressures, with the majority of weight concentrated in the heel and the

foot. Therefore, the piezoelectric signals measured in the heel and sole are stronger. Flexible piezoelectric sensors can be used to develop hand or foot movement monitoring equipment. This approach can yield significant benefits if applied in intelligent wearable devices, such as controllers with gesture-based inputs, prosthetics, and other applications. Generally speaking, flexible piezoelectric sensors are widely used in medicine, health monitoring, and intelligent wearable technology.

Conclusion

We for the first time found the piezoelectric properties of FPI and fabricated a series of FPI electrospun nanofiber membranes. The fabricated FPI nanofibers exhibit outstanding thermal stability with a thermal decomposition temperature of 550 °C and T_g of ~260 °C. Moreover, the electrostatic spinning of FPI leads to the formation of nanofiber membranes with distinguishable piezoelectric properties. The polarization effect of fluorine-containing functional groups can further enhance the piezoelectric signal. The FPI sensor prepared in this work can generate piezoelectric signals above 10 V under external excitation and be used as the power supply device for wearable devices. It can quickly respond and recover to external stimuli in 15 ms, and its sensitivity is measured to be 478.72 mV N^{-1}. Under excitation and after 10 000 cycles, the output can remain stable and has the potential for long-term operation. In addition, FPI has excellent moisture and water resistance with a superhydrophobicity of 139.59°, which facilitates its stability in complex circumstances for application in a wearable sensor. This work offers a promising candidate for developing high-temperature-resistant nanofibers and piezoelectric nanofibers, which could significantly contribute to advancing high-temperature-resistant flexible wearable devices for energy harvesting in extreme environments.

Author contributions

Liangkang Huang: writing – original draft, writing – review and editing, and data curation. Jianwei Li: conceptualization, supervision, and project administration. Shuting Chen: visualization. Bilin Zhang: software. Shengping Li: investigation. Wei Fan: formal analysis. Qiangli Zhao: funding acquisition. Xuman Wang: resources.

Data availability

Data will be made available on request from the author.

Conflicts of interest

The authors declare that they have no conflict of interest.

Acknowledgements

The authors would like to acknowledge the support of the National Advanced Functional Nanofiber Innovation Center (2020-fx020009), Xi'an Science and Technology Plan Project (23GXFW0015), and Xi'an Science and Technology Plan Project (23ZDCYJSGG0032-2022).

References

1 W. Linping and L. Run-Wei, *Science*, 2024, **383**, 1416.
2 J. Hao, W. Li, J. Zhai and H. Chen, *Mater. Sci. Eng., R*, 2019, **135**, 1–57.
3 R. Tu, B. Zhang and H. A. J. N. E. Sodano, *Nano Energy*, 2022, **97**, 107175.
4 R. Bai, H. Shao, H. Chang, H. Wang, X. Ding, W. Cao, Y. Cao and T. Lin, *J. Mater. Chem. A*, 2023, **11**, 26230–26241.
5 G. Hu, X. Zhang, X. Liu, J. Yu and B. Ding, *Adv. Fiber Mater.*, 2021, **3**, 14–25.
6 L. Li, Z. Zheng, C. Ge, Y. Wang, H. Dai, L. Li, S. Wang, Q. Gao, M. Liu, F. Sun and T. Zhang, *Adv. Mater.*, 2023, **35**, 2304099.
7 J. Tao, Y. Wang, X. Zheng, C. Zhao, X. Jin, W. Wang and T. Lin, *Nano Energy*, 2023, **118**, 108987.
8 L. Lu, X. Liu, Y. Sun, S. Wang, J. Liu, S. Ge, T. Wei, H. Zhang, J. Su, Y. Zhang and W. Fan, *Adv. Mater.*, 2024, **36**, 2308748.
9 H. Li, J. Li, W. Chu, J. Lin, J. Xin, F. Liu, Z. Li and Z. Ma, *ACS Appl. Nano Mater.*, 2024, **7**, 7783–7793.
10 W. Chu, J. Li, J. Lin, W. Li, J. Xin, F. Liu, X. He, Z. Ma and Q. Zhao, *Compos. Sci. Technol.*, 2024, **249**, 110489.
11 J. Park, Y. w Lim, S. Y. Cho, M. Byun, K. I. Park, H. E. Lee, S. D. Bu, K. T. Lee, Q. Wang and C. K. Jeong, *Small*, 2022, **18**, 2104472.
12 Z.-X. Huang, L.-W. Li, Y.-Z. Huang, W.-X. Rao, H.-W. Jiang, J. Wang, H.-H. Zhang, H.-Z. He and J.-P. Qu, *Nat. Commun.*, 2024, **15**, 819.
13 W. Lian, L. Wang, J. Wang, T. Cheng, K. Dai, B. Lu, C. Liu, C. Pan and C. Shen, *Adv. Funct. Mater.*, 2024, 2404403, DOI: 10.1002/adfm.202404403.
14 T. Han Huang, F. Kenneth, C. Espino, X.-Y. Tian, J. Widakdo, H. Faye, M. Austria, O. Setiawan, W.-S. Hung, K. Ray, S. Pamintuan, R. Balasadas Leron, C.-Y. Chang, A. R. Caparanga, K.-R. Lee and J.-Y. Lai, *Chem. Eng. J.*, 2024, **487**, 150569.
15 W. Fan, R. Lei, H. Dou, Z. Wu, L. Lu, S. Wang, X. Liu, W. Chen, M. Rezakazemi, T. M. Aminabhavi, Y. Li and S. Ge, *Nat. Commun.*, 2024, **15**, 3509.
16 J. Guo, Q. Wu, C. Zhang, Y. Li, M. Nie, Q. Wang and Y. Liu, *Mater. Des.*, 2022, **217**, 110616.
17 L. Song, Z. Huang, S. Guo, Y. Li and Q. Wang, *ACS Appl. Mater. Interfaces*, 2021, **13**, 37252–37261.
18 M. Kanik, O. Aktas, H. S. Sen, E. Durgun and M. Bayindir, *ACS Nano*, 2014, **8**, 9311–9323.
19 R. Yin, Y. Li, W. Li, F. Gao, X. Chen, T. Li, J. Liang, H. Zhang, H. Gao, P. Li and Y. Zhou, *Nano Energy*, 2024, **124**, 109488.
20 Y. Fu, J. Liu, J. Zou, S. Xu, Y. Wei, W. Zhang and D. Li, *Chem. Eng. J.*, 2024, **489**, 151495.
21 Y. Huang, S. Chen, Y. Li, Q. Lin, Y. Wu and Q. Shi, *Chem. Eng. J.*, 2024, **488**, 150997.

22 G. Mohana Rani, K. S. Ranjith, S. M. Ghoreishian, A. T. E. Vilian, C. Roh, R. Umapathi, Y.-K. Han and Y. S. Huh, *Adv. Fiber Mater.*, 2024, 1–14, DOI: **10.1007/s42765-024-00453-1**.
23 Y. Zheng, W. Wang, J. Niu, X. Jin, Y. Sun, L. Peng, W. Li, H. Wang and T. Lin, *Nano Energy*, 2022, **95**, 106995.
24 W. Song, C. Xie, G. Yang, M. Zhang, K. Su, J. Li and Z. Li, *Chem. Eng. J.*, 2024, **490**, 151698.
25 M. Jia, C. Yi, Y. Han, L. Wang, X. Li, G. Xu, K. He, N. Li, Y. Hou, Z. Wang, Y. Zhu, Y. Zhang, M. Hu, R. Sun, P. Tong, J. Yang, Y. Hu, Z. Wang, W. Li, W. Li, L. Wei, C. Yang and M. Chen, *Adv. Sci.*, 2022, **9**, 2105738.
26 T. Jia, Z. Fan, S. Zheng, H. Zhou, H. Chen, N. Ma and C. Liu, *Chem. Eng. J.*, 2024, **492**, 152230.
27 B. C. Wyatt, S. K. Nemani, G. E. Hilmas, E. J. Opila and B. Anasori, *Nat. Rev. Mater.*, 2023, 1–17, DOI: **10.1038/s41578-023-00619-0**.
28 S. Eswarappa Prameela, T. M. Pollock, D. Raabe, M. A. Meyers, A. Aitkaliyeva, K.-L. Chintersingh, Z. C. Cordero and L. Graham-Brady, *Nat. Rev. Mater.*, 2022, **8**, 81–88.
29 Y. Wang, Y. Cui, Z. Shao, W. Gao, W. Fan, T. Liu and H. Bai, *Chem. Eng. J.*, 2020, **390**, 124623.
30 X. Tiantian, Z. Chenyu, F. Xueling, W. Qamar, F. Wei and L. Tianxi, *Adv. Fiber Mater.*, 2022, **4**, 1118–1128.
31 G. Jian, Y. Jiao, Q. Meng, Y. Guo, F. Wang, J. Zhang, C. Wang, K.-S. Moon and C.-P. Wong, *Nano Energy*, 2021, **82**, 105778.
32 J. Lin, J. Li, Y. Song, W. Chu, W. Li, F. Liu, X. He, Q. Zhao and H. Zhao, *ACS Appl. Mater. Interfaces*, 2024, **16**, 16712–16723.
33 X. Tao, S. Li, Y. Shi, X. Wang, J. Tian, Z. Liu, P. Yang, X. Chen and Z. L. Wang, *Adv. Funct. Mater.*, 2021, **31**, 2106082.
34 J. Li, X. Zhang, Y. Lu, K. Linghu, C. Wang, Z. Ma and X. He, *Adv. Fiber Mater.*, 2021, **4**, 108–118.
35 S. Osali, Y. ghiyasi, H. Esfahani, R. Jose and S. Ramakrishna, *Mater. Today*, 2023, **67**, 151–177.
36 D. Ji, Y. Lin, X. Guo, B. Ramasubramanian, R. Wang, N. Radacsi, R. Jose, X. Qin and S. Ramakrishna, *Nat. Rev. Methods Primers*, 2024, **4**, 1.
37 X.-X. Wang, G.-F. Yu, J. Zhang, M. Yu, S. Ramakrishna and Y.-Z. Long, *Prog. Mater. Sci.*, 2021, **115**, 100704.
38 M. G. Dhara and S. Banerjee, *Prog. Polym. Sci.*, 2010, **35**, 1022–1077.
39 H. Chen, J. Huang, C. Zhang, P. Gao, H. Huang, J. Li and J. Liu, *Chem. Eng. J.*, 2024, **490**, 151598.
40 B. Wan, M. Xiao, X. Dong, X. Yang, M. S. Zheng, Z. M. Dang, G. Chen and J. W. Zha, *Adv. Mater.*, 2023, 2304175, DOI: **10.1002/adma.202304175**.
41 Y. Yu, W. Zhu, H. Li, J. Long, W. Huang, J. Li, L. Chen and Y. Zhang, *Eur. Polym. J.*, 2024, **203**, 112653.
42 M. Li, Z. Wu, X. Chen, F. Gan, C. Teng, X. Li, J. Dong, X. Zhao and Q. Zhang, *Chem. Eng. J.*, 2024, **486**, 150255.
43 D. Gubała, A. Slastanova, L. Matthews, L. Islas, P. Wąsik, F. Cacho-Nerin, D. Ferreira Sanchez, E. Robles, M. Chen and W. H. Briscoe, *ACS Nano*, 2024, **18**, 5940–5950.
44 X. Du, Y. Liu, S. Mo, L. Zhai, M. He, L. Fan, Y. Wang, W. Zhao and G. Wang, *Composites, Part B*, 2024, **273**, 111262.
45 S. Park, Y. So, K. Woong Kim, J. Park, H. Kim, L. Kyung Kim, J. Kim, H.-T. Jung, D. Woo Kim, J. Chan Won and Y. Ho Kim, *Chem. Eng. J.*, 2024, **495**, 153288.
46 Y. Meng, S. Xing, N. Wu, P. Zhang, X. Cui, X. Liang and S. Wang, *ACS Mater. Lett.*, 2024, **6**, 1457–1466.
47 Y. Chen, Y. He, Y. Gao, J. Xue, W. Qu, J. Xuan and Y. Mo, *Science*, 2024, **384**, 670–676.
48 L. Chen, S. Mei, K. Fu and J. Zhou, *ACS Nano*, 2024, **18**, 15358–15386.
49 K. S. Ogueri and C. T. Laurencin, *ACS Nano*, 2020, **14**, 9347–9363.
50 J. Xiong, L. Wang, F. Liang, M. Li, Y. Yabuta, M. A. Iqbal, G. Mayakrishnan, J. Shi and I. S. Kim, *Adv. Fiber Mater.*, 2024, 1–17, DOI: **10.1007/s42765-024-00415-7**.
51 J. Lin, J. Li, W. Li, S. Chen, Y. Lu, L. Ma, X. He and Q. Zhao, *Composites, Part A*, 2024, **178**, 108003.
52 J. Yan, M. Liu, Y. G. Jeong, W. Kang, L. Li, Y. Zhao, N. Deng, B. Cheng and G. Yang, *Nano Energy*, 2018, **56**, 662–692.
53 S. Kilper, T. Jahnke, M. Aulich, Z. Burghard, D. Rothenstein and J. Bill, *Adv. Mater.*, 2018, **31**, 1805597.
54 Y. Wang, J. Li, W. Chu, K. Chen, Z. Ma, F. Liu and Q. Zhao, *ACS Appl. Mater. Interfaces*, 2024, **16**, 56116–56125.
55 H. Li, J. Li, W. Chu, J. Lin, P. He, W. Fan and Q. Zhao, *Compos. Sci. Technol.*, 2024, **257**, 110820.
56 L. Kong, W. Li, T. Zhang, H. Ma, Y. Cao, K. Wang, Y. Zhou, A. Shamim, L. Zheng, X. Wang and W. Huang, *Adv. Mater.*, 2024, **36**, 2400333.